



**HAL**  
open science

## High-Entropy-Alloy Nanocrystal Based Macro- and Mesoporous Materials

Maria Letizia de Marco, Walid Baaziz, Sharmin Sharna, François Devred, Claude Poleunis, Alexandre Chevillot-Biraud, Sophie Nowak, Ryma Haddad, Mateusz Odziomek, Cédric Boissière, et al.

► **To cite this version:**

Maria Letizia de Marco, Walid Baaziz, Sharmin Sharna, François Devred, Claude Poleunis, et al.. High-Entropy-Alloy Nanocrystal Based Macro- and Mesoporous Materials. ACS Nano, 2022, 16 (10), pp.15837-15849. 10.1021/acsnano.2c05465 . hal-03862002

**HAL Id: hal-03862002**

**<https://hal.science/hal-03862002>**

Submitted on 20 Nov 2022

**HAL** is a multi-disciplinary open access archive for the deposit and dissemination of scientific research documents, whether they are published or not. The documents may come from teaching and research institutions in France or abroad, or from public or private research centers.

L'archive ouverte pluridisciplinaire **HAL**, est destinée au dépôt et à la diffusion de documents scientifiques de niveau recherche, publiés ou non, émanant des établissements d'enseignement et de recherche français ou étrangers, des laboratoires publics ou privés.

## High Entropy Alloys Nanocrystals Based Macro and Mesoporous Materials

*Maria Letizia De Marco, Walid Baaziz, Sharmin A. Sharna, François Devred, Claude Poleunis, Alexandre Chevillot-Biraud, Sophie Nowak, Ryma Haddad, Mateusz Odziomek, Cédric Bossière, Damien P. Debecker, Ovidiu Ersen, Jennifer Peron,\* Marco Faustini\**

### Abstract

High-Entropy Alloys (HEA) nanoparticles are attractive for several applications in catalysis and energy. Great efforts are currently devoted to establish composition-property relationships to improve catalytic activity or selectivity. Equally importantly, developing practical fabrication methods for shaping HEA-based materials into complex architectures is a key requirement for their utilization in catalysis. However, shaping nano-HEA into hierarchical structures avoiding demixing or collapse remains a great challenge. Herein, we overcome this issue by introducing a simple soft-chemistry route to fabricate ordered macro- and mesoporous materials based on HEA nanoparticles, with high surface area, thermal stability and catalytic activity toward CO oxidation. The process is based on spray-drying from aqueous solution containing five different noble metal precursors and polymer latex beads. Upon annealing, the polymer plays a double role: templating and reducing agents enabling formation of HEA nanoparticles-based porous networks at only 350°C. The formation mechanism and the stability of the macro- and mesoporous materials were investigated by a set of *in-situ* characterization techniques; notably, *in-situ* Transmission Electron Microscopy unveiled that the porous structure is stable up to 800°C. Importantly, this process is green, scalable and versatile and could be potentially extended to other classes of HEA materials.

Keywords: high entropy alloys, polymer templated synthesis, aerosol synthesis, porous materials, catalysis



Multi-principal element alloys, composed of five or more homogeneously mixed metals in nearly equimolar ratios, are known as high entropy alloys (HEAs).<sup>1-4</sup> The term refers to the high configurational entropy of these solid solutions, which pushes the mixing free energy towards negative values, allowing the mixing of metals that are normally immiscible in binary and ternary alloys.<sup>1,5,6</sup> According to the literature, high entropy alloys can be defined based on their configurational entropy or based on their composition. The entropy-based definition requires an entropy higher than  $1.61R$ .<sup>7</sup> The composition-based definition is more extensive, including every multi metallic alloy composed of at least five elements ranging between 5% and 35% in atomic concentration.<sup>3,4</sup> According to this definition, every quinary alloy with mixing entropy between  $1.36R$  and  $1.61R$  is a HEA. A compromise between these two definitions is found by defining any alloy with mixing entropy equal or higher than  $1.5 R$  a high entropy alloy.<sup>1,7</sup> Although the concept of multicomponent alloys with high configurational entropy has been known for nearly thirty years,<sup>4,8</sup> there is a recent growing interest in such materials due to their enormous potential in heterogeneous catalysis and electrocatalysis.<sup>1,9</sup> Their reportedly high chemical and thermal stability, combined with the possibility to finely tune the active sites reactivity by adjusting the alloy composition, make HEAs the ideal playground for the design of new catalysts.<sup>1,2,5,9-12</sup> Ammonia decomposition,<sup>5</sup> carbon oxide oxidation,<sup>13</sup> carbon dioxide reduction,<sup>14</sup> hydrogen<sup>2,15,16</sup> and oxygen<sup>16,17</sup> evolution reaction, are some examples of catalytic and electrocatalytic applications of HEAs. Due to the increasing importance of HEAs in catalysis and electrocatalysis, a large number of fabrication strategies has been recently reported. They all address the common challenge of fabricating stable, homogeneous solid-state solutions, composed of at least 5 elements. This is commonly achieved by rapidly heating the precursors to a very high temperature ( $1000^{\circ}\text{C}$  or above), followed by fast quenching.<sup>13,16-19</sup> For instance, carbothermal shock is successfully used to fabricate supported nano-HEA particles.<sup>18</sup> Spray pyrolysis is an alternative approach allowing the scalable synthesis of micrometric, unsupported, spherical HEAs particles composed of several immiscible metals.<sup>19,20</sup> Nano-HEAs particles ( $<2$  nm) can also be produced by co-sputtering different metals into ionic liquids.<sup>21</sup> Several groups managed to synthesize nano-HEAs by conventional wet-chemistry or solvothermal methods, which considerably reduce the energetic cost of HEAs production, but often involve the use of toxic or flammable solvents.<sup>2,10,22,23</sup>

Besides, processing and shaping HEAs into architected materials relevant for catalytic applications is still an important challenge in the field. As demonstrated for other family of materials in the past decades (oxides, carbon, hybrids)<sup>24</sup> introducing porosity at different

scales is of outmost importance for catalytic applications to maximize active surface area and optimize matter transport.<sup>25,26</sup> Therefore, the realization of porous HEAs with elevated specific surface area is highly desirable. The fabrication of porous HEAs is arduous with the top-down and bottom-up approaches currently available. So far, mesoporous HEA have only been realized by arc-furnace melting of a multimetallic Al-based ingot containing traces of several metals (for instance  $\text{Al}_{97.5}\text{Ni}_{0.5}\text{Cu}_{0.5}\text{Pt}_{0.5}\text{Pd}_{0.5}\text{Au}_{0.5}$ ) followed by post-synthesis treatment with NaOH to remove Al.<sup>13,16,17</sup>

In this paper, we introduce a simple soft-chemistry route to fabricate ordered macro- and mesoporous materials based on HEA nanoparticles, with high surface area, thermal stability and catalytic activity toward CO oxidation. The synthesis is inspired by the templated sol-gel synthesis of porous metal oxides *via* spray-drying,<sup>27-31</sup> a waste-free, “green”, easily scalable technique. It is particularly successful for the synthesis of powdery heterogeneous oxide catalysts with an excellent control of texture, composition, and surface properties.<sup>32</sup> Beyond oxides, our group recently showed that this approach can be transferred to the synthesis of porous metal or metal alloys particles.<sup>33</sup> In this paper, we significantly raise the level of chemical and structural complexity achievable by aerosol synthesis by fabricating HEA-based particles with controlled meso- or hierarchical macro- and mesoporosity (see scheme in **Figure 1**). Mesoporous and hierarchical macro- and mesoporous HEA-based particles were prepared using five platinum group metals (PGM) of crucial importance in the field of catalysis and electrocatalysis: Pt, Pd, Rh, Ru and Ir.<sup>2,11,22,34</sup> Characterization techniques such as *in-situ* mass and infrared spectroscopy, *in-situ* and scanning electron microscopy, were used to study the formation mechanism and thermal stability of hierarchically porous HEA-based particles, showing that thermally stable, fully metallic HEA-based porous particles can be obtained in mild conditions, without resorting to extreme synthesis temperatures. Due to their porous architecture, these materials exhibit enhanced catalytic performances toward CO oxidation, opening interesting perspectives for the application of HEAs in catalysis and electrocatalysis.

## Results and discussion

### Methodology for the preparation of porous HEAs

As illustrated in the scheme in **Figure 1**, the fabrication process is operationally simple but mechanistically more complex. Metal chloride precursors of the five noble metals ( $\text{RuCl}_3 \cdot x\text{H}_2\text{O}$ ,  $\text{RhCl}_3 \cdot x\text{H}_2\text{O}$ ,  $\text{IrCl}_3 \cdot x\text{H}_2\text{O}$ ,  $\text{PtCl}_4$  and  $\text{PdCl}_2$ ) were dissolved in nearly equimolar concentrations in deionized water and mixed with an aqueous suspension of polymer latex to

obtain a latex-to-metal *ratio* of 50 wt. %. The spray-drying process generates, by solution atomization, an aerosol of droplets containing the latex particles and the dissolved metal chlorides salts. Upon water evaporation, the droplets are further converted into hybrid spheroidal microparticles. The resulting microparticles are composed of the organic latex beads embedded in the inorganic metal chloride salts matrix (**Figure S1** and **Figure S4**). Upon thermal annealing under Ar, the polymer latex template decomposes resulting in the formation of mesoporous or macroporous nanostructured microparticles, with pore size depending on the diameter of polymer template beads employed. In our case, porous nanostructured microparticles, composed of Pt, Pd, Ru, Rh and Ir were obtained by spray-drying using two different types of latex particles as templating agents: polystyrene (PS) or polymethyl methacrylate (PMMA) beads (Figure 1).

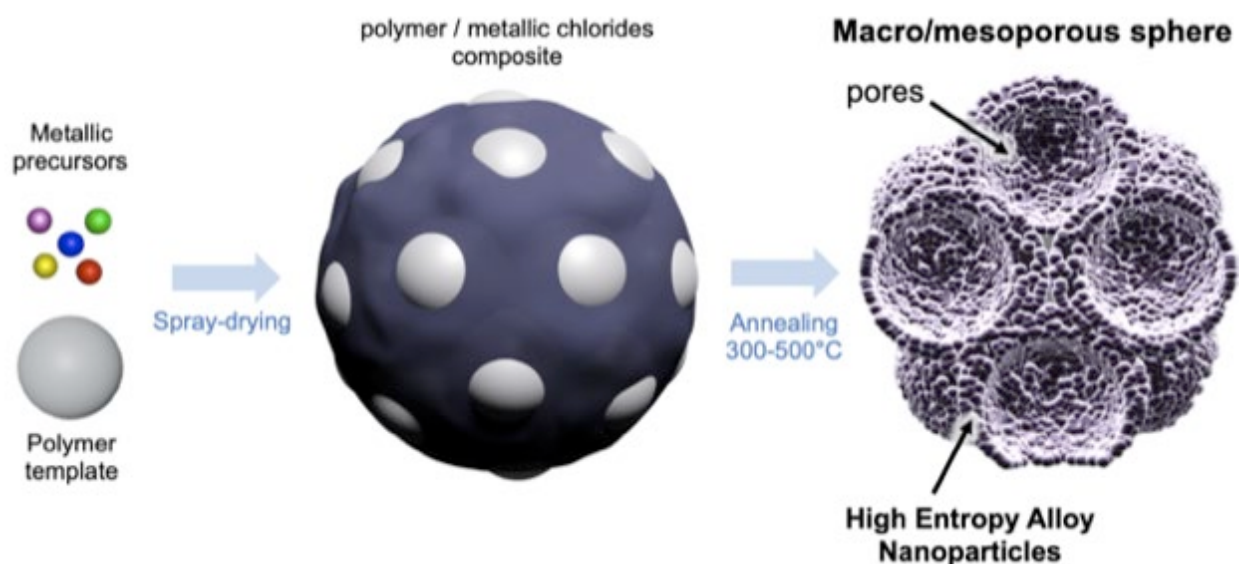


**Figure 1:** Scheme of the fabrication process of porous HEA-based particles by aerosol synthesis followed by thermal annealing

### Synthesis of mesoporous HEAs

To produce mesoporous HEA-based particles, polystyrene (PS) beads of *ca.* 30 nm were used as templating agent (**Figure 2**). The calcination under inert atmosphere (Ar) at 500 °C yielded polydisperse mesoporous microparticles with an irregular “*deflated*” shape and pore size of *ca.* 20-30 nm, as shown in Figure 2 A and **Figure S1** and **S2** A-D. Scanning transmission electron microscopy (STEM) shows that the pore walls are actually composed of crystalline nanoparticles of *ca.* 4-5 nm (see Figure 2B, C and F, and S2 E-F). The X-ray diffraction

pattern (XRD) of the mesoporous sample corresponds to a single face centered cubic (fcc) metal phase (XRD in Figure 2 C). The presence of a unique crystalline phase supports the formation of a homogeneous solid solution, and therefore the formation of a high entropy alloy.

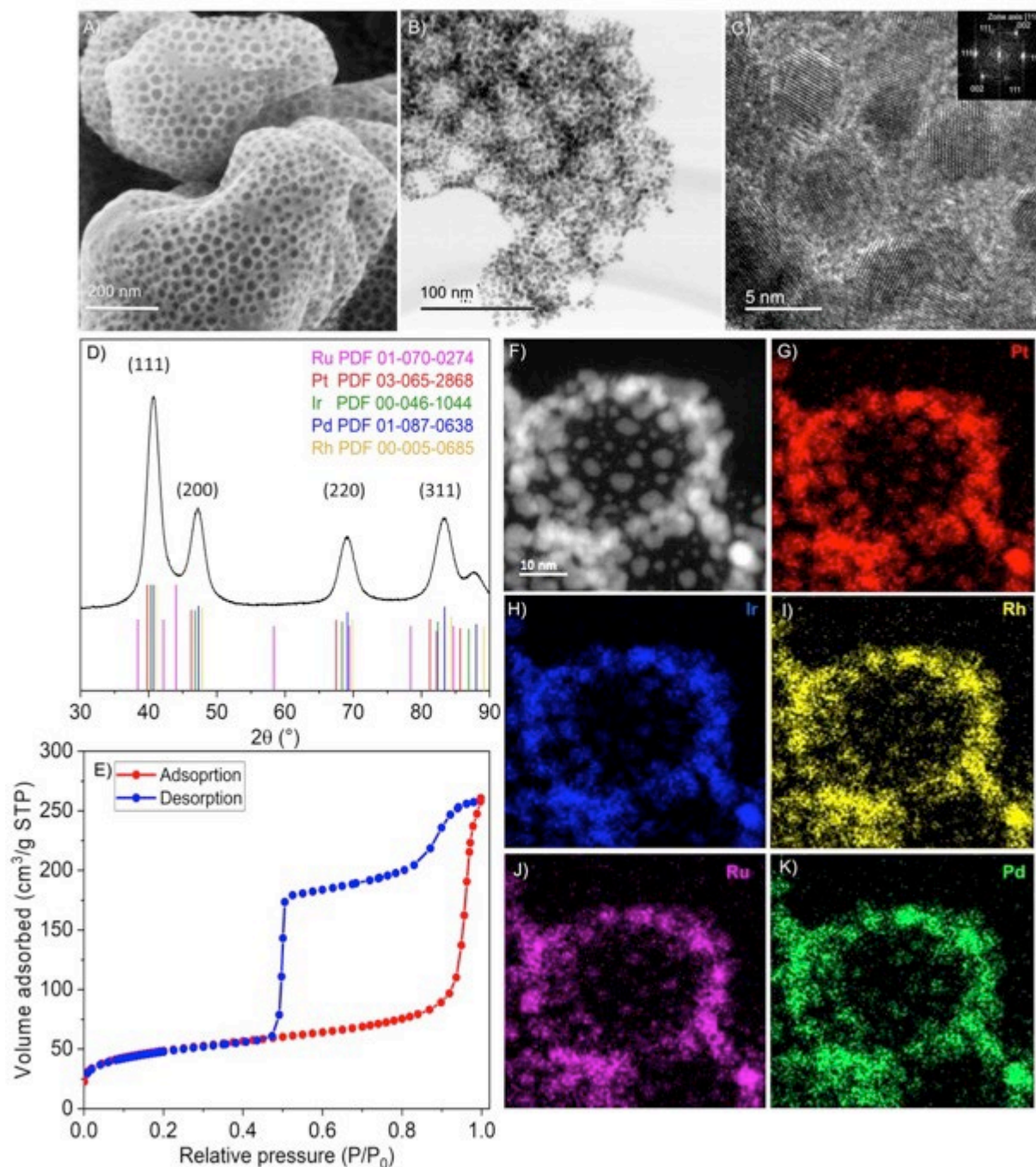


**Figure 2:** High entropy alloy (HEA) based mesoporous particles annealed at 500 °C. SEM pictures of the mesoporous HEA-based particles surface (A). STEM (B), and high-resolution STEM images (C). The inset in Figure 2C is the Fast Fourier transform (FFT) of the nanocrystal in the dotted frame. X-Ray diffraction pattern, which corresponds to a face centered cubic (fcc) structure (D). N<sub>2</sub> adsorption-desorption isotherms (E). STEM image of a

mesoporous HEA-based particle (F) and the elemental mapping (STEM-EDX) showing the distribution of Pt (red, G), Ir (blue, H), Rh (yellow, I), Ru (pink, J) and Pd (green, K).

The full width at half maximum of the diffraction peaks (FWHM) corresponds to a crystallite size of about 3.5 nm. Peaks broadening can be also due to the alloying between the five metals, which might result in a distortion of the fcc lattice. Elemental mapping performed by scanning transmission electron microscopy coupled with energy dispersive X-ray spectroscopy (STEM-EDX, in Figure 2F-J) indicates that the five metals are homogeneously mixed throughout the whole porous structure.

High resolution STEM images in **Figure 3** A-D evidence that the nanoparticles composing the mesoporous particles are single nanocrystals with size  $\leq 5$  nm, with a fcc cubic structure (see also Figure 2 C). The interplanar distance of 2.2 Å evidenced in Figure 3B corresponds to the (111) family of planes in the fcc structure. High resolution STEM-EDX (Figure 3 E-J) confirms that each single nanocrystal is a HEA composed of five, homogeneously mixed PGM, supporting the conclusions drawn by XRD analysis. These combined results support the hypothesis that HEA nanocrystal-based mesoporous particles are obtained by templated aerosol synthesis followed by thermal annealing.

The porosity and specific surface area of the mesoporous particles have been characterized by N<sub>2</sub> adsorption. The N<sub>2</sub> adsorption and desorption isotherms feature a type IV hysteresis loop, characteristic of capillary condensation in monodisperse mesopores with bottleneck openings (Figure 2D).<sup>35</sup> The shape of the adsorption curve suggests the presence of micropores, as confirmed by the t-plot (see **Figure S3** A). Microporosity can in part be attributed to residual residual carbon, generated during the annealing step under Ar. The presence of carbon is confirmed by Raman spectroscopy; the two large Raman peaks detected at 1350 cm<sup>-1</sup> and 1590 cm<sup>-1</sup> correspond to the benzene rings breathing mode and to the stretching mode of sp<sup>2</sup> bonds in disordered graphitic carbon respectively (**Figure S4** in Supporting).<sup>36,37</sup>

The pore size distribution, determined with the Barret, Joyner and Halenda (BJH) model on the desorption branch of the hysteresis presents two distinct bumps, corresponding to N<sub>2</sub> desorption from pores or restrictions of different size. The pore size distribution calculated from the desorption branch shows two populations of pores or restrictions, of 17 nm and 6.5 nm. The signals at 17 nm and 6.5 nm might be attributed to the bottle-neck restrictions and to openings in the pore walls connecting the mesopores.

A specific surface area of 150 m<sup>2</sup>/g was determined using the Brunauer-Emmett-Teller (BET) method. This is a remarkably high specific surface area considering the high density of Pt-

group metals and represents a record in the field HEAs, the second highest value reported in the literature being  $56.8 \text{ m}^2/\text{g}$ .<sup>16</sup> In summary, mesoporous microparticles, composed of homogeneous HEAs nanocrystals and characterized by a high specific surface area, are easily produced in relatively mild conditions by templated aerosol synthesis.

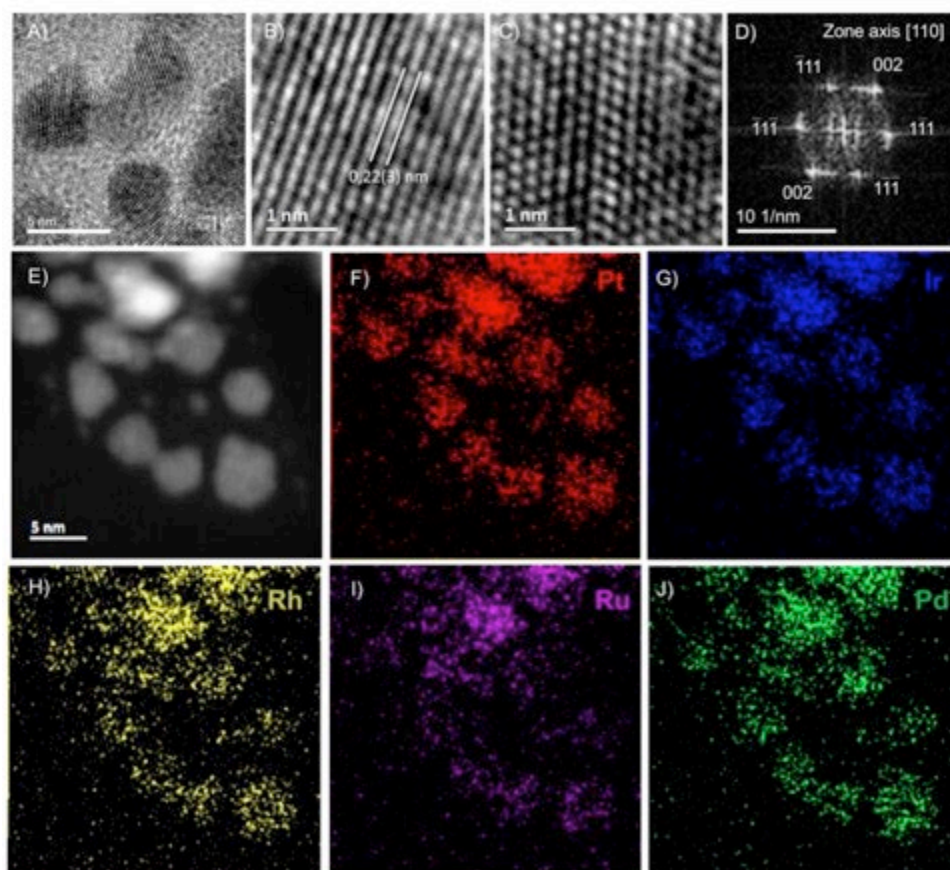


**Figure 3:** High resolution STEM characterization of the HEA nanocrystals composing the mesoporous particles. High resolution image (A) and details of the crystalline planes (B and C), FFT of the crystalline lattice in 3C (D). STEM image (E) and elemental mapping showing the distribution of Pt in red (F), of Ir in blue (G), of Rh in yellow (H), of Ru in pink (I) and of Pd in green (J) within a group of nanocrystals.

### Synthesis of hierarchical macro- and mesoporous HEAs

Being highly flexible, this templated synthesis presents the possibility to easily “select” the pore size by simply adjusting the size of the latex template beads. Macroporous HEA-based particles were prepared using a synthesis protocol identical to that reported for the mesoporous HEA-based particles, except that the PS latex templating particles were replaced with monodisperse polymethylmethacrylate (PMMA) beads of *ca.* 300 nm (**Figure 4**).

The thermal annealing of the as-sprayed PMMA-templated hybrid particles under inert gas (Ar) at 500 °C yields macroporous particles with monodisperse, ordered pores of *ca.* 200 nm (Figure 4A). The macropores form a hexagonal close-packed (hcp) structure (Figure 4B). Such pattern is induced by water evaporation during the spray-drying process, which leads to the self-assembly of the PMMA latex beads in a hcp structure. The PMMA templated macroporous particles do not exhibit the “deflated” morphology characteristic of the mesoporous particles. This difference is already present in the hybrid pristine particles before annealing, as can be observed by comparing the SEM images in **Figure S6** and S1. Probably, the PS latex particles are too small to support the spheroidal superstructure, which collapses forming a “deflated” superstructure. Conversely, the larger PMMA particles are capable of forming self-sustaining spheroidal superstructures.

Since the PMMA has a lower degradation temperature than PS,<sup>38</sup> we studied the effect of lower annealing temperatures on particles crystallinity and morphology, by XRD (Figure 4B and **Figure S7**) and SEM (**Figure S8**). Five additional temperatures were explored: 450 °C, 400 °C, 350 °C, 300 °C and 250 °C. Before annealing, pristine, as sprayed particles are mainly amorphous. The large bumps at  $\sim 35^\circ$  and  $\sim 51^\circ$  in the XRD pattern can be attributed to amorphous  $\text{RhCl}_3$ ,<sup>39</sup> while the sharp peaks detected at  $35.7^\circ$  and  $36.7^\circ$  can be assigned to the  $\text{PdCl}_2$  and  $\text{RuCl}_3$  precursors respectively.<sup>40,41</sup> These results indicate that the chloride salts are neither decomposed nor reduced during the spray-drying step. At 250 °C, the signals corresponding to the fcc phase are detected: this is the onset of metal crystallization. However, at this temperature, another signal can be observed at  $15.5^\circ$ , which can be attributed either to residual chloride precursors ( $\text{RhCl}_3$  or  $\text{RuCl}_3$ )<sup>39,40</sup> or to the PMMA latex template<sup>42,43</sup> (Figure S7A). The SEM characterization confirms that the PMMA latex beads are still present in the samples annealed at 250 °C (Figure S8 A-C).

XRD patterns corresponding to a single fcc phase are observed for particles annealed at 300 °C and above. The XRD peaks become sharper with increasing annealing temperature (Figure 4C and S7A in Supporting). This is correlated with the crystallites size, which increases from 2.8 nm, for samples annealed at 300 °C, to 4.0 nm, for samples annealed at 500 °C. The slight shift at lower angles ( $\sim 0.5^\circ$ ) observed for sample annealed at 300 °C might be explained with the incomplete reduction of the metal salts. The particles morphology is not significantly affected by the annealing temperature (see Figure S8). Similarly to the mesoporous particles, the pore walls of the macroporous particles are composed by small nanocrystals with a fcc symmetry. (see Figure 4E and Figure S9 A-E). The elemental mapping obtained by STEM-EDX indicates that all the elements are homogeneously mixed

throughout the porous structure forming a HEA (Figure 4 F-J). As in the case of the mesoporous particles, high resolution STEM-EDX shows that each individual nanocrystal is actually a HEA crystal composed of the five Pt-group metals (see Figure S9 H-L).

The N<sub>2</sub> adsorption and desorption isotherms for the particles annealed at 500 °C exhibit a curve characteristic of macroporous materials with no *plateau* at high partial pressures (Figure 4D). The presence of a hysteresis with a desorption in between 0.68 and 0.47 P/P<sub>0</sub> suggests the presence of mesoporous restrictions in between the macropores.<sup>35</sup> The pore size distribution, calculated from the desorption branch with the BJH model (see Figure S3 D in Supporting), shows the presence of restrictions of about 5.4 nm. Such restrictions could be attributed to small openings connecting the macropores, or to interstitial spaces among the HEA nanocrystals forming the macroporous sample (see Figure S9 G). A second peak at 4 nm could be attributed to catastrophic desorption. The specific surface area determined with the BET method is 103 m<sup>2</sup> g<sup>-1</sup>, lower than the specific surface area of PS-templated mesoporous HEAs, but still considerably high if compared to the values obtained for mesoporous HEAs by Al de-alloying of arc-melted ingots.<sup>13,16</sup> In this case, the presence of micropores is not revealed by the t-plot (see Figure S3B). In summary, PMMA templated HEA-based particles present a hierarchical porosity, characterized by large (~200 nm) macropores with mesoporous restrictions within the macropores walls.

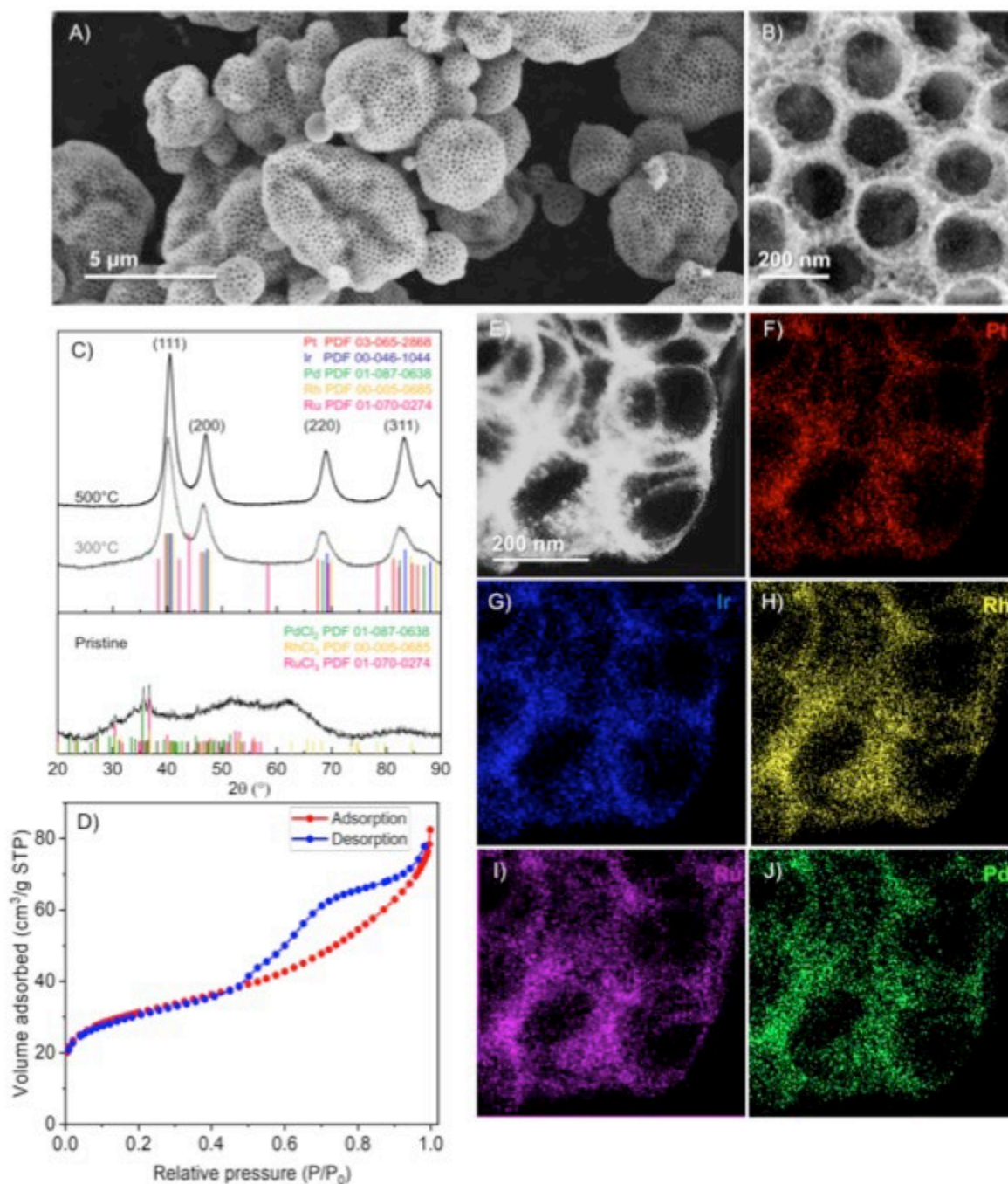


**Figure 4:** Morphology and composition of the hierarchical macro- and mesoporous HEA particles. SEM images (A, B), XRD pattern of the as-sprayed particles (pristine), and of the particles annealed at 300 °C and 500 °C under Ar (C). N<sub>2</sub> adsorption and desorption isotherms of the hierarchical meso- and macroporous particles (D). STEM-EDX image (E) and elemental mapping (F-J) of a hierarchical meso- and macroporous particle.

A set of complementary characterization techniques has been employed in order to reinforce the conclusion drawn from STEM-EDX and XRD characterization, and ascertain that the porous, nanostructured particles fall indeed into the definition of high entropy alloys (**Figure**

5). Figure 5A shows the elemental compositions for the hierarchical macro- and mesoporous particles determined by X-ray fluorescence spectroscopy (XRF) and energy dispersive X-ray spectroscopy (SEM-EDX). The two techniques are in excellent agreement, indicating that all the metals are comprised between 5% and 35% in atomic concentration. The mixing entropy calculated from the EDX and XRF results is in both cases 1.58 R. The porous particles fall within both the composition-based and entropy-based definition for HEAs.

In order to probe the mixing among the different metals at the *atomic scale* we performed time of flight secondary ion mass spectroscopy (ToF-SIMS). This analysis relies on the bombardment of the sample surface with a pulsed primary ion beam (here  $\text{Bi}_5^+$ ) and on the analysis of the emitted secondary ions by high resolution time-of-flight mass spectroscopy. Here, the analysis of a pure Ru reference sample allowed detecting the expected  $\text{Ru}^+$ ,  $\text{Ru}_2^+$ ,  $\text{Ru}_3^+$ ,  $\text{Ru}_4^+$  ions (the representative example of  $\text{Ru}_3^+$  is shown in Figure 5B). The assignment is unambiguous, owing to the natural isotopic distribution of Ru and to the high mass resolution of the spectra. In the hierarchical macro- and mesoporous HEA sample, the expected ions related to the presence of Ru, Pd, Pt, Rh, and Ir are also observed (with 1 to up to 5 metal atoms of the same element in the clusters). Importantly, the spectra of the HEA-based particles also present patterns that are not assignable to monometallic clusters but have to be attributed to mixed metallic clusters such as  $\text{RuPd}^+$ ,  $\text{RuPt}^+$ ,  $\text{Ru}_2\text{Pt}^+$ ,  $\text{RuIr}^+$ ,  $\text{Ru}_2\text{Ir}^+$ ,  $\text{Ru}_2\text{Pd}^+$ ,  $\text{Rh}_2\text{Ru}^+$ ,  $\text{RuRhPt}^+$ ,  $\text{RuRhIr}$ ,  $\text{RuRhPd}^+$ ,  $\text{Ru}_3\text{Pt}^+$ , *etc.* For some of these possible mixed clusters, the theoretical isotopic distributions overlap, preventing any unambiguous assignment. However, in some parts of the spectra the molecular signature of some mixed clusters can be identified unambiguously. Figure 5B shows the representative example of  $\text{RuPt}^+$  and  $\text{Ru}_2\text{Rh}^+$ . In summary, the only pattern that emerges in this part of the spectrum for the Ru reference is the one of  $\text{Ru}_3^+$ . In the hierarchical porous HEA-based particles, the pattern of  $\text{Ru}_3^+$  is possibly present as well, but it is clearly accompanied by other patterns that can be assigned to  $\text{RuPt}^+$  (with a possible contribution of  $\text{RhPt}^+$  and  $\text{RuIr}^+$ ) and  $\text{Ru}_2\text{Rh}^+$  (with a possible contribution of  $\text{Rh}_2\text{Ru}^+$ ) clusters. The detection of these signals constitutes a qualitative but definitive proof that the spray-drying preparation indeed led to a true alloying with intimate mixing of the metal elements, not only at the nanoscale as visualized by STEM-EDX, but also at the atomic level. The ToF-SIMS characterization provided a definitive proof of the alloying in the HEA-based particles.

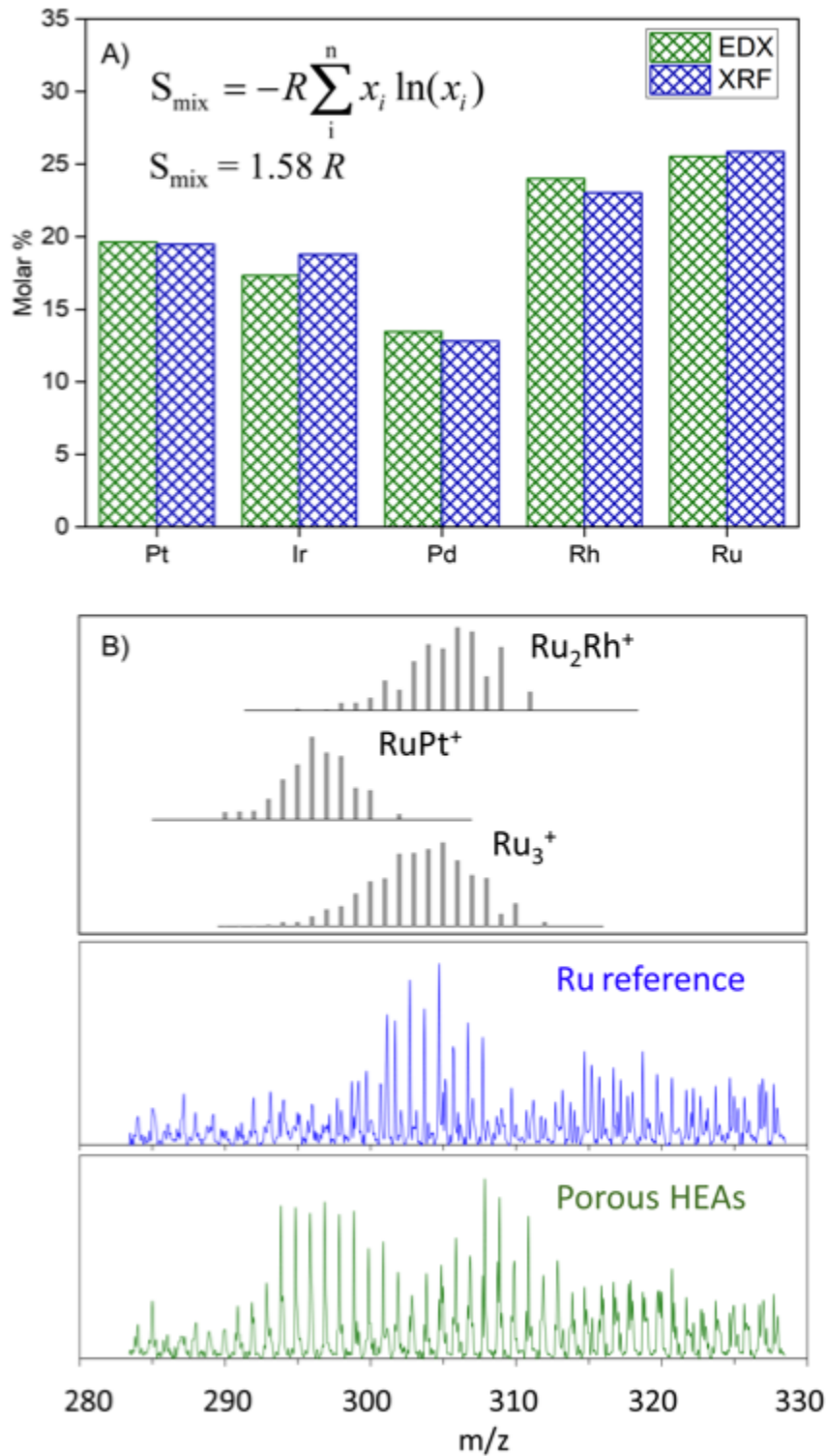


**Figure 5:** Atomic composition of HEA-based macro and mesoporous hierarchical particles. Atomic composition determined by X-ray fluorescence spectroscopy (XRF) and energy dispersion X-ray spectroscopy (EDX) (A). Part of the ToF-SIMS spectrum obtained on the macro- and mesoporous HEA-based particles (green) and on a reference Ru-based macroporous reference particle (blue). Histograms (grey) represent the theoretical isotopic distribution for Ru<sub>3</sub><sup>+</sup>, RuPt<sup>+</sup>, and Ru<sub>2</sub>Rh<sup>+</sup>.

### **Role of the polymer template on the formation of porous HEAs**

Thermal decomposition of noble metal chlorides into pure metals under inert atmosphere typically occurs at temperatures higher than 300 °C (for instance, the decomposition of  $\text{IrCl}_3 \cdot x\text{H}_2\text{O}$  to Ir occurs above 600 °C). Nevertheless, in our previous work we have shown that PMMA latex particles can serve as bi-functional templating and reducing agent for porous noble metals.<sup>33</sup> Here, to prove the reducing activity of PMMA in the case of the porous HEA-based particles, control samples were prepared according the same protocol, but without PMMA template, and annealed under exactly the same conditions at 300 °C, 350 °C, 400 °C, 450 °C and 500 °C (see Figure S6 B in Supporting).

*Role of the polymer on phases segregation.* In the absence of the PMMA latex template, the XRD pattern of the sample annealed at 300°C shows small peaks which can be unambiguously assigned to the fcc phase, however the main phases detected are characteristics of  $\text{PdCl}_2$  precursor (peak at  $\sim 35.4^\circ$ ),<sup>41</sup>  $\text{RhCl}_3$  and  $\text{RuCl}_3$  (broad shoulders at about  $15.5^\circ$ ,  $35^\circ$  and  $50^\circ$ -  $60^\circ$ ) (Figure S7 B).<sup>39,40</sup> By increasing the annealing temperature, both the signals corresponding to the metal fcc phase and the peaks corresponding to the metal chlorides increase in intensity. For samples annealed at 450 °C without PMMA, we still observe a mixture of metallic fcc phase and metal chlorides peaks. The peaks of the fcc phase are not symmetric, and present a shoulder towards the high angles, which might indicate that perfect alloying is not obtained without PMMA template. At 500 °C, the metal chloride peaks are no longer observed, however, a small signal at  $2\theta \sim 43^\circ$  appears along with the fcc phase signals. This signal may be assigned to the reflection of the (101) planes of the hcp phase,<sup>44</sup> *i.e.* the phase in which pure ruthenium typically crystallizes. Probably, ruthenium, or more likely a Ru-rich hcp phase, segregates at 500 °C.<sup>23,44-46</sup> These results suggest that the PMMA template triggers the low temperature reduction and crystallization of the porous HEA-based particles, and simultaneously hinders metals de-alloying at high annealing temperatures.

*Role of the polymer on metal reduction.* Both the series of PMMA-templated materials and un-templated materials have been characterized by X-ray photoelectron spectroscopy (XPS) to probe the oxidation state of metal atoms and the surface composition (see **Figure S10** and **Figure S11**). For templated particles, full conversion of metal chlorides to metals is obtained by annealing under Ar at 350 °C and above, while samples annealed at 300 °C are only partially reduced (Figure S10). In light of this observation, the slight shift to lower diffraction angles observed in XRD for the sample annealed at 300 °C might be explained with its partial reduction. The reduction step from 300 °C to 350 °C is accompanied by a substantial loss of

chlorine atoms, as determined by the elemental quantifications by XPS (see Figure S12, and Tables S1 and S2). Conversely, non-templated reference particles annealed at 400 °C are fully composed of metal chlorides, and reduction to metals only occurs above 450 °C (Figure S11). The carbon-to-metals *ratio* of hierarchically porous particles annealed at 450 °C was estimated to be about 0.65, corresponding to a carbon concentration of and 5% *wt.* (details about the calculation are reported in Supporting). This result is in agreement with the Raman spectroscopy, indicating that the porous particles contain carbon, generated upon polymer degradation under inert atmosphere. From the combination of the XRD, XPS, and SEM results, we can confirm that the PMMA latex has a double function and acts both as a templating and reducing agent at low annealing temperature, as shown for pure metal and bimetallic materials.<sup>33</sup> The same reducing effect is observed with PS too, as shown in Figure S5.

In order to gain a deeper understanding of the PMMA-driven reduction mechanism of HEAs particles, we conducted a thermogravimetric study of the annealing process, coupled with *in-situ* gas chromatography mass spectrometry (GC-MS) and infrared spectroscopy (FTIR) of the volatile species engendered (**Figure 6**). The thermogravimetric analysis (TGA) profile obtained by heating the pristine PMMA-templated powders under an Ar flow at a rate of 5 °C/min, shows a gradual mass loss up to 150 °C that can be attributed to the loss of water contained in the pristine powder (Figure 6A). The small step observed around 260 °C-270 °C might correspond to the cleavage of unsaturated end groups of the PMMA latex.<sup>33</sup> An abrupt mass loss occurs between 300 °C and 400 °C, reducing the mass of the sample to 40% of its initial mass. Halfway these two temperatures, at *ca.* 350 °C, the slope of the TGA curve changes, becoming less abrupt. Above 400°C the mass loss is much slower, at 800 °C the mass is reduced to the 30% of the initial mass.

The total ion count recorded as a function of the temperature obtained by TGA coupled with GC-MS analysis is presented in Figure 6B. The different molecular fragments, differentiated according to their *m/z ratio* are also presented. The ion flow in the chromatogram reaches its maximum between 300 °C and 400 °C, in agreement with the considerable mass loss observed by TGA. Based on the TGA and chromatogram data, we identified the temperatures at which important phenomena occur, and extracted from the chromatogram the mass and IR spectra corresponding to 300 °C, 330 °C, 350 °C, 400 °C and 450 °C (**Figure S13** and **Figure S14** in Supporting).

A fragment with *m/z* 36, corresponding to HCl, is released in a narrow interval of time between 300 °C and 350 °C, with a peak at 330 °C. Above 350 °C the HCl is no longer

detected, in correspondence with the change of the slope of the TGA curve in Figure 6A. Therefore, we can suppose that the change of the slope is due to the cessation of HCl evolution.

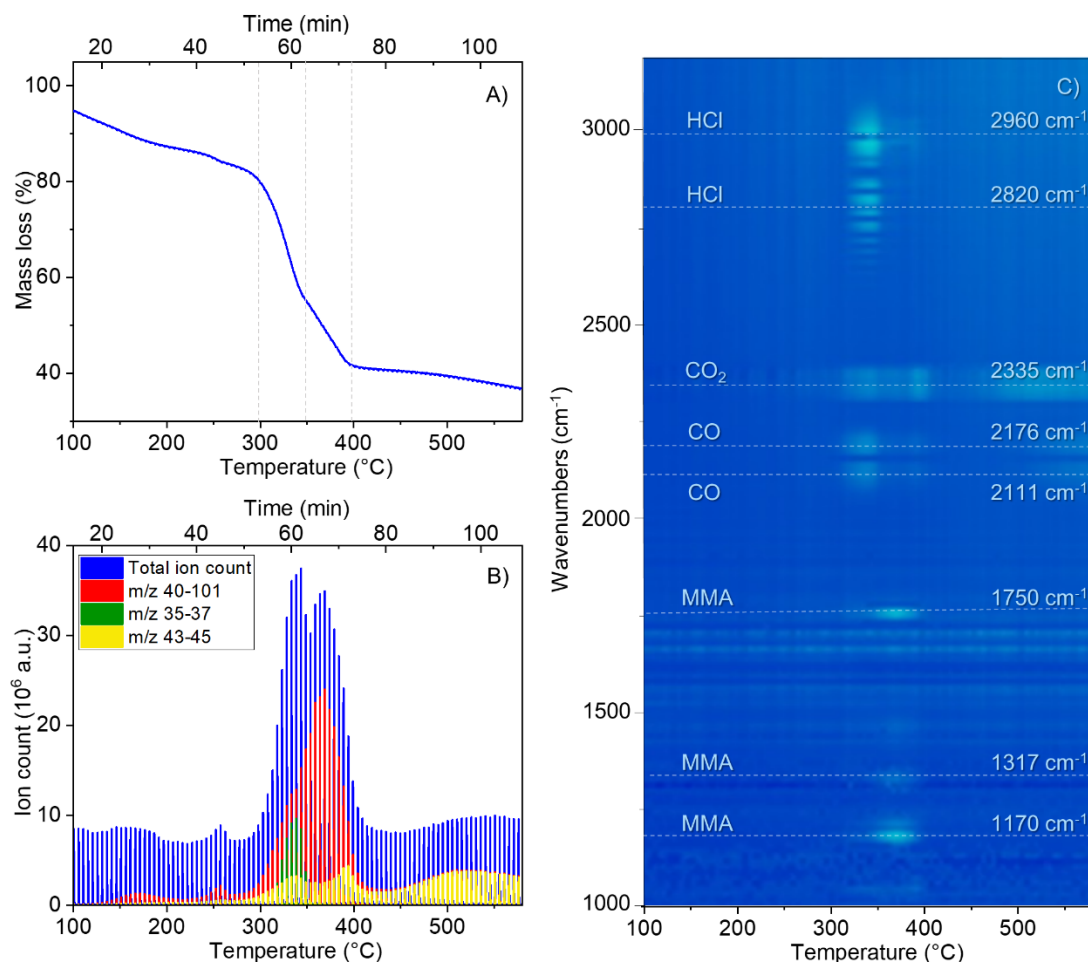


**Figure 6:** Analysis of the formation mechanism of hierarchical macro- and mesoporous HEA based particles. TGA analysis of the pristine particles annealed under inert atmosphere with a heating rate of 5 °C/min (A). Gas phase mass chromatogram of the volatile products engendered by TGA including total ion count (blue) and selected m/z region with m/z comprised between 35 and 37 in green, m/z comprised between 43 and 45 in yellow and m/z comprised between 40 and 101 in red (B). 3D infrared spectrum of the volatile species (C).

Fragments with m/z ratio of 41, 69 and 100 are detected between 330 °C and 400 °C, with a maximum at 365 °C. The fragment with m/z 100 corresponds to the mass of the methylmetacrylate (MMA), *i.e.*, the monomer forming the PMMA latex template. The two fragments of m/z 41 and 69 m/z are characteristics of its fragmentation (see Figure S14 C).<sup>33</sup> Since we can detect the entire MMA monomer, we can assume that the PMMA latex template

decomposes mostly by radical depropagation. The decomposition starts at about 160 °C. The small peak detected at 160 °C is attributed to the cleavage of head-to-head groups;<sup>33</sup> the first of three steps for the radical depolymerization of PMMA. The second small peak appearing at *ca.* 260 °C is due to the scission of the unsaturated groups at the end of the chains. The third and most intense peak appearing at *ca.* 320 °C and reaching a maximum at 365 °C corresponds to the depropagation reaction, by random scission of the PMMA chains.<sup>33</sup>

These conclusions are strengthened by the IR spectra performed on the volatile products of thermal annealing. The 3D IR spectrum in Figure 6C represents the evolution of the IR spectra as a function of the time of analysis. The IR signals intensity is plotted *versus* the wavenumber (on the *y*-axis) and the temperature (on the *x*-axis). A gradation of blue indicates the intensity of the IR signals, where the lighter the color the higher the intensity. As a support for the analysis of the 3D IR spectrum, a series of IR regular spectra, taken at the same temperatures mentioned above (300 °C, 350 °C, 400 °C, and 450 °C), are showed in Figure S13 and in more details in Figures S14 A-B.

Below 300 °C, we can only observe a series of thin lines centered at 1500 and 1700  $\text{cm}^{-1}$  which can be associated to the bending vibration of  $\text{H}_2\text{O}$ ,<sup>47</sup> and a weak band at 2335  $\text{cm}^{-1}$  corresponding to the  $\text{CO}_2$  stretching. The  $\text{CO}_2$  stretching intensifies at 300 °C, and new signals centered at 2111  $\text{cm}^{-1}$  and 2176  $\text{cm}^{-1}$ , corresponding to the stretching vibration of CO, appear. Above 300 °C we observe the development of two intense bands centered at 2960 and 2820  $\text{cm}^{-1}$ ; which correspond to the rotovibrational IR signal of the HCl molecule.<sup>33</sup> The spectra in Figure S14 A-B show in details the rotovibrational structure of gaseous CO and HCl. HCl is no longer detected above 350 °C. The signals at 1170 and 1317  $\text{cm}^{-1}$ , typical of  $\alpha$ - $\beta$  unsaturated esters,<sup>48</sup> and the signal at 1750  $\text{cm}^{-1}$ , typical of the stretching vibration of the carbonyl moiety,<sup>48</sup> are characteristic of the MMA monomer and arise at about 320 °C-330 °C. These signals increase in intensity up to 400 °C and are no longer observed after 450 °C (see Figure S13). Therefore, the depropagation reaction of PMMA by random chain scission occurs in a narrow interval of time, between 320°C and 400 °C, following the evolution of HCl. Above 400 °C only  $\text{CO}_2$ , CO and  $\text{H}_2\text{O}$  are detected by IR and mass spectrometry.

We can conclude that the formation of hierarchical macro- and mesoporous HEA-based particles proceeds *via* a two-step mechanism: the metal chlorides reduction and the PMMA depropagation. As already demonstrated for single noble metal particles or binary alloys,<sup>33</sup> the polymer template plays a key-role in the metal precursor reduction. Alkyl radicals reduce the metal chlorides by reacting with the chlorine atom and releasing it in the form of hydrochloric acid. The reduction of the metal chlorides to metals occurs between 300 °C and 350 °C. As

shown by Raman spectroscopy, residual carbon is also generated upon polymer degradation under inert atmosphere. Once the metal chlorides are fully reduced, residual PMMA chains decompose by random chain scission through radical depolymerization. These two steps are partially superimposed; we observe, in fact, that the PMMA depropagation occurs even below 330 °C, when the MS signal from the HCl reaches its maximum value. Carbon oxide and carbon dioxide can be also issued from this reduction process, as the oxidized products of the radical reaction, or can be produced by an alternative reduction path, such as the one suggested by Gayard *et al.* in their study about the formation of mesoporous noble metals films.<sup>49</sup>

In summary, porous latex-templated HEA-based particles can be fully reduced and crystallized at relatively low annealing temperatures (350 °C for the PMMA-templated macro- and mesoporous particles and 500 °C for PS-templated mesoporous particles). These results represent a significant advancement in the synthesis of HEAs, showing that spray-drying is a valuable technique for the facile bottom-up production of porous HEA-based particles.

### **Catalytic activity and thermal stability of HEA-based porous particles**

Porous metals and alloys are of great technological interest for catalysis and electrocatalysis applications, as they combine both intrinsic catalytic properties of metals and an increased specific surface area with an easy access to active surface sites.<sup>26,50</sup> The porous HEA-based particles that we developed contain noble metals (Rh, Pt and Pd) commonly used in automotive three ways catalysts (TWC) for the reduction of toxic exhaust fuels emissions. The oxidation of CO to CO<sub>2</sub> is one of the three main catalytic reactions occurring in TWC, and is one of great technological interest not only to reduce toxic gas emissions but also to remove CO from the reformed gas containing H<sub>2</sub> for fuel cell applications.<sup>51–53</sup> Therefore, in order to unveil the benefits of the porous architecture, we chose CO oxidation as the ideal model reaction to test the catalytic activity of porous HEA-based materials. We also run reference tests without catalysts and with non-porous reference particles having the same chemical composition as the porous HEA-based particles. The catalytic tests were performed in a fixed bed micro-reactor, under a continuous flow of CO and O<sub>2</sub>, as detailed in the Experimental section.

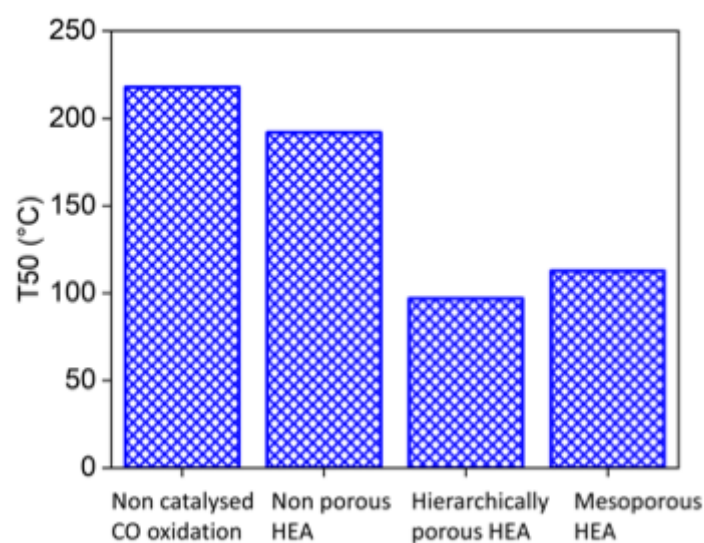


**Figure 7.** Catalytic activity of hierarchically porous (macro- and mesoporous) and mesoporous HEA-based particles, annealed at 500 °C, towards CO oxidation (expressed as the temperature at which 50% CO conversion is reached, T<sub>50</sub>), compared with non-porous particles having the same composition (continuous flow of CO and O<sub>2</sub>).

The results in **Figure 7** show that both the hierarchical macro- and mesoporous and the mesoporous HEA-based particles exhibit an enhanced catalytic activity towards CO oxidation, compared to the non-porous reference. The CO half conversion temperature, T<sub>50</sub>, is 97 °C and 113 °C for the hierarchically porous and mesoporous HEA-based particles respectively, and 192 °C for the non-porous reference, which shows poor activity in the CO oxidation reaction, being close to the blank reaction. Complete conversion of CO to CO<sub>2</sub> occurs at 100 °C for the hierarchical meso- and macroporous particles and at 115 °C for the mesoporous particles (**Figure S15**). Based on the BET determined specific surface area, one would expect the mesoporous HEAs to be more active than the hierarchically porous HEAs. This discrepancy is possibly due to the higher amount of graphitized carbon on the HEAs surface prepared with PS, hindering the access of the CO molecules to the active sites on the surface. However, with both the hierarchically porous and mesoporous catalysts, the temperature for complete CO oxidation is reduced by more than 100 °C, compared to the non-catalyzed reference reaction (blank reaction, **Figure S15**). This is encouraging, considering that commercial TWC systems typically become active between 250 °C and 400 °C.<sup>53,54</sup> Thermal stability is another important requirement for real applications.<sup>53-55</sup> For instance, supported gold nanoparticles are very active catalysts for CO oxidation, exhibiting a good conversion rate at room

temperature and below.<sup>54,56</sup> However, at high working temperature, Au nanoparticles tend to aggregate and become inactive.<sup>53,54</sup>

We investigated the thermal stability of the hierarchical meso- and macroporous HEA-based particles at high temperature and under non-reactive conditions by *in-situ* STEM-EDX (Figure 8). HEA-based particles originally annealed at 300 °C were heated in a closed TEM cell up to 900 °C. In order to fit in the support for the in-situ analysis, the HEA porous material was grinded and only a fragment was observed while heating. STEM images and STEM-EDX elemental mappings were taken at different temperatures in order to follow the evolution of particles morphology and homogeneity with increasing temperature.

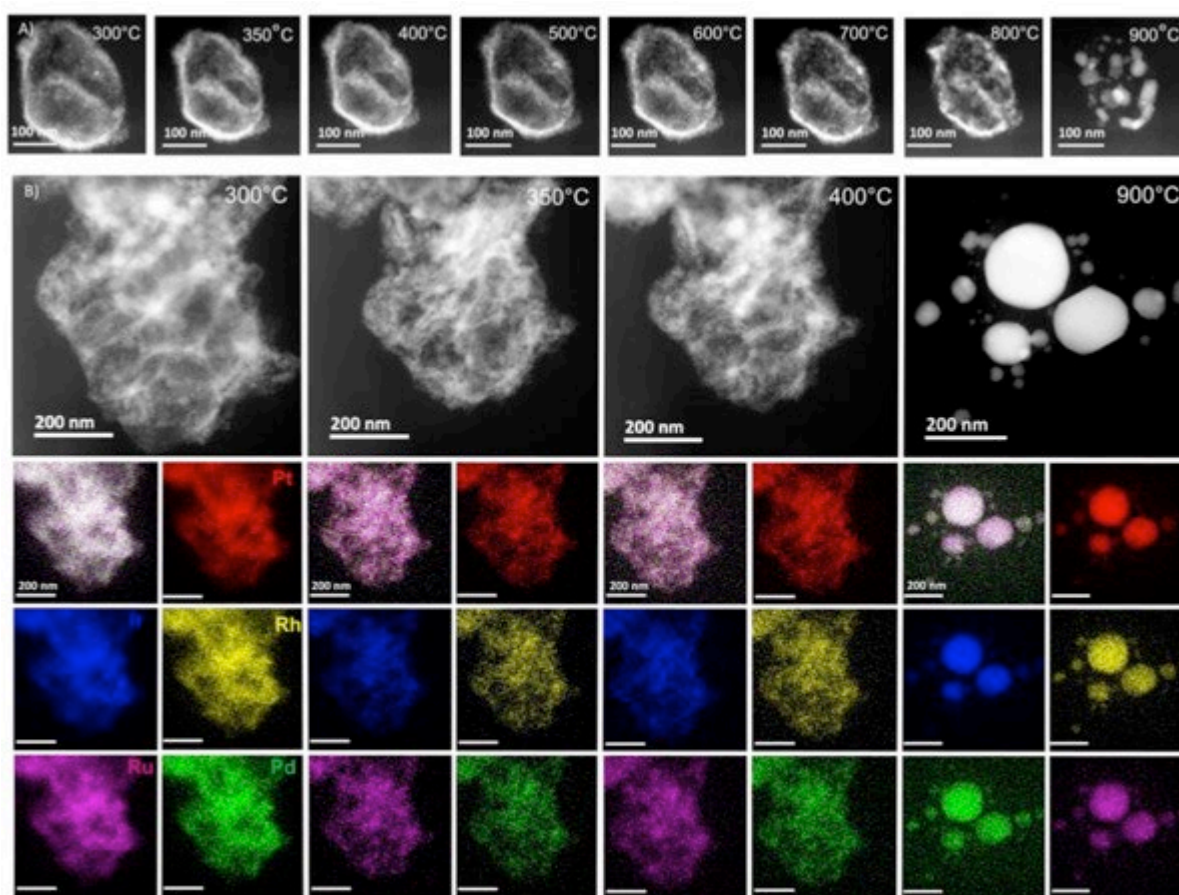


**Figure 8.** Thermal stability of the porous HEA-based particles. *In situ* STEM of a fragment of hierarchical macro- and mesoporous HEA-based particle (A), and *in situ* STEM and EDX mapping of a hierarchical meso- and macroporous HEA-based particle (B) at different temperatures under a flow of Ar.

As shown in Figure 8, the particles shrink when heated from 300 °C to 350 °C, in correspondence to the loss of HCl and the completion of metal chloride reduction. Above

350 °C and up to 800 °C the porous structure is preserved; and no major changes are observed, except for a significant increase in crystallites size between 600 °C and 800 °C. At 900 °C the porous structure is completely lost. The EDX elemental mapping shows that the annealing temperature does not alter the homogeneous distribution of the elements throughout the porous structure, and even when the porous structure is destroyed at 900 °C, the particles are still composed of homogeneously mixed elements. In summary, this analysis proved that hierarchical meso- and macroporous HEA-based porous particles are stable up to 800 °C, and maintain a homogeneous mixing among the elements up to 900 °C.

This proof of concept suggests that HEA-based porous catalysts, featuring high chemical and thermal stability, combined with the possibility of include very active metals in the alloys might respond to both the requirements of activity and high thermal stability for thermal catalysis applications.

## Conclusion

As demonstrated for other class of materials in the past decades (oxides, carbon, hybrids) introducing porosity at different scales is of utmost importance for catalytic applications. In this work, we introduce a porous architecture for HEA: ordered mesoporous and hierarchical meso/macroporous HEAs based nanocrystals made of 5 noble metals, synthesized by soft-templating approaches. This green and scalable approach based on spray-drying does not require extremely high process temperature, or the use of flammable or toxic organic solvents, contrarily to other common approaches for HEAs.<sup>2,13,18,19</sup> We thoroughly characterized these porous materials with a set of *in-situ* and *ex-situ* characterization techniques. SEM and STEM-EDX analysis showed that the porous HEA-bases particles are composed of small nanocrystals (~4 nm) made of homogeneously mixed Pt-group metals. From a fundamental point of view, the complex formation mechanism of the PMMA-templated hierarchical macro- and mesoporous HEA-based particles was unveiled by *in-situ* IR and GC-MS, performed on the volatile products generated upon thermal gravimetry analysis. In agreement with previous literature,<sup>33</sup> we show that the polymer latex template is responsible for the reduction of metal precursors in mild conditions. In addition, our analyses suggest that the presence of the polymer template hinders atom diffusion and de-alloying during the thermal treatment, “freezing” the alloy in its high entropy state and therefore allowing for the formation of nanostructured HEAs with homogeneous composition. *In situ* TEM analysis revealed that the porosity of HEA-based particles is thermally conserved up to 800 °C without phase segregation. Finally, the catalytic activity of the HEAs has been tested for the carbon

oxide oxidation reaction, a process of crucial importance for reducing the toxic emissions of car motors. Both hierarchical macro- and mesoporous HEA-based particles and mesoporous HEA-based particles show enhanced activity for CO oxidation and higher chemical stability compared to non-porous reference particles with the same chemical composition. It is important to underline that the current porous materials contain residual carbon that might modify their catalytic activity and stability compare to bare HEA nanocrystals. The role of the carbon cannot currently be disentangled from that of the HEA. One perspective of this work will consist in understanding the carbon-HEA interplay for catalysis by synthesizing carbon-free porous HEAs. Beyond that, this versatile approach will potentially allow the exploration of new self-supported HEA-based materials with even more sophisticated architectures and chemical composition, with important implications in catalysis and electrocatalysis.

### **Experimental Section/methods**

*Materials:* Palladium chloride ( $\text{PdCl}_2$  96%), platinum chloride ( $\text{PtCl}_4$  99%), iridium chloride hydrate ( $\text{IrCl}_3 \cdot x\text{H}_2\text{O}$ ) and ruthenium chloride hydrate ( $\text{RuCl}_3 \cdot x\text{H}_2\text{O}$ ) were purchased from Sigma Aldrich, rhodium chloride hydrate ( $\text{RhCl}_3 \cdot x\text{H}_2\text{O}$ ) was purchased from Alfa Aesar. Pluronic (F127), methyl methacrylate and styrene monomers were purchased from Sigma Aldrich. Deionized water was obtained with a MiliQ system.

*Latex synthesis:* Polymethylmethacrylate (PMMA) latex beads with a diameter of 300 nm were produced following the protocol published by Hutton and co-workers.<sup>57</sup> The PMMA latex suspension has a concentration of 11% in weight in water.

Polystyrene (PS) latex beads with a diameter of 30 nm were produced as follows: 5 g of Pluronic (F127) were dissolved in deionized water (200 g), in a three-neck flask connected to a refrigerating column. Styrene monomer (13 g) and  $\text{NaHCO}_3$  (0,440 g) were added to the flask under vigorous magnetic stirring (700 rpm). The solution was bubbled with a flux of nitrogen for 40 minutes to remove the oxygen. In a separate flask, potassium persulfate (0,44 g) was dissolved in water (15g), this solution was degassed with nitrogen for 10 minutes, and then added to the three-neck flask. The temperature was brought to 90°C and the reaction carried out for 5 hours.

The PS latex was washed by centrifuging 3 times at 10000 rpm for 30 minutes. The latex colloidal suspension was then dialyzed against distilled water, the dialyzed was changed each 12 hours, for six times. The PS latex suspension has a concentration of 6% in weight in water.

*High entropy alloy-based particles synthesis:* Five stock solutions were prepared, containing each individual metal chloride precursor in deionized water. Individual stock solutions of  $\text{RhCl}_3 \cdot x\text{H}_2\text{O}$ ,  $\text{RuCl}_3 \cdot x\text{H}_2\text{O}$ ,  $\text{IrCl}_3 \cdot x\text{H}_2\text{O}$  and  $\text{PtCl}_4$  were prepared by dissolving 0.150 g of each metal salt in 60 g of water (0.25 % of metal precursor in weight). A stock solution of  $\text{PdCl}_2$  was prepared by dissolving 0.130 g of salt in 130 g of deionized water (0.1 % of  $\text{PdCl}_2$  in weight). Concentrated HCl (0.12 mL of 37% HCl) was added to the  $\text{PdCl}_2$  solution, obtaining a pH between 1 and 2, in order to help the dissolution of the salt. The  $\text{PdCl}_2$  solution was then filtered with a cellulose acetate syringe filter (0.2  $\mu\text{m}$ ), to remove the remaining aggregates.

Equal volumes of each stock solution (30 mL) were mixed in a glass jar under magnetic stirring. A suspension of latex (PMMA or PS) was added to the solution in order to obtain a latex-to-metal salts *ratio* of 50% in weight.

The suspension was stirred for 15 minutes and then sprayed using a B-290 mini spray-dryer from Büchi. The nozzle temperature was set to 150°C, the air flow to  $\sim 8 \text{ L min}^{-1}$  and the suspension flow to  $3 \text{ mL min}^{-1}$ . The aspirator flow rate was set to  $0.45 \text{ L min}^{-1}$ . Pristine powders were annealed in a tubular oven under a flow of Ar. The oven was purged with Ar for one hour to remove the oxygen and avoid the oxidation of the metals. The ramp rate was set to  $5^\circ\text{C min}^{-1}$ , and the powders were annealed at the desired temperature for a dwelling time of 5 minutes. Powders were annealed at 300°C, 350°C, 400°C, and 450°C.

Reference samples, containing all the five metal precursors mixed together, but not the latex, were produced at the same time, to monitor the effect of the latexes on the structuration and phase of the HEA powders.

*X-Ray diffraction:* X-Ray diffraction pattern were performed using a powder diffractometer D8 Advance from Bruker, equipped with a Cu anode (1.54 Å) and operating at 40 kV and 30 mA. Powder diffractograms were recorded in a  $2\theta$  range between  $10^\circ$  and  $90^\circ$ , with a  $0.039^\circ$  step size and a step acquisition time of 2 seconds.

*Nitrogen sorption analysis:* the  $\text{N}_2$  sorption studies and specific surface area measurements were carried out at 77 K using a Micromeritics ASAP 2010 instrument. The Brunauer-Emmett-Teller (BET) method was applied to determine the specific surface area from the nitrogen adsorption data. The BET specific surface area was calculated in the relative pressure range of 0.05–0.30, according to the criteria described by Rouquerol *et al.*<sup>35</sup>

*Scanning electron microscopy (SEM):* Scanning electron microscopy was carried out on powders deposited onto a conductive carbon tape support, using a SU-70 Hitachi FESEM, equipped with a Schottky emission gun as source of electrons. The images were obtained with an accelerating voltage of 5kV for the annealed samples and 1 kV for not annealed samples, and a filament current of 65  $\mu$ A. The working distance was set 7 mm.

*Scanning electron microscopy coupled with energy dispersive X-ray spectroscopy (SEM-EDX):* The analysis of the elemental composition (EDX) was performed on a ZEISS Gemini SEM 360 equipped with an Oxford Instruments Ultim Max 170 mm<sup>2</sup> detector. SEM images and EDX mapping were obtained by Inlens SE detector (In Column) at 5 kV accelerating voltage. Oxford Instrument AZtec software was used for the acquisition of EDX maps, point & ID analysis.

*Energy dispersive X-ray fluorescence (EDXRF):* Elemental analyses of the powders were conducted by EDXRF using an epsilon 3XL spectrometer from Panalytical equipped with a silver X-ray tube. The calibration was performed by depositing a mass in the range 5–20  $\mu$ g of the standard solution of each element on a polycarbonate membrane. The same conditions were adopted for all samples (50 kV and 6  $\mu$ A). The detection limits for Pt, Pd, Ru, Rh and Ir were determined to be 14.8, 96.1, 25.9, 83.1 and 19.5 ng, respectively.

*Scanning transmission electron microscopy (STEM) and energy dispersive X-ray spectroscopy (EDX):* Experiments were performed using a JEOL 2100 FEG S/TEM microscope operated at 200 kV equipped with a spherical aberration probe corrector (Cs from CEOS), high resolution objective lens pole piece and an UltraScan 1000 CCD array detector (GATAN). The samples were deposited on a holey carbon coated TEM grid. For high-angular annular dark field (HAADF) analysis, we used a spot size of 0.13 nm, a current density of 140 pA, a camera focal length of 8 cm, corresponding to inner and outer diameters of the annular detector of about 73 and 194 mrad. Elemental analyses were carried out in STEM mode with an energy dispersive X-ray spectroscopy (EDX) probe using a silicon drift detector (SDD) with a sensor size of 60 mm<sup>2</sup>.

*In situ STEM-EDX:* For the *in situ* observations, a Protochips Atmosphere system was used; which is based on sandwiching the sample between two micro-electro-mechanical systems (MEMS) based closed cells made up of transparent SiN<sub>x</sub> (for observation) and SiC films (for

heating).<sup>58</sup> The sample was grinded and suspended in ethanol. One drop (1  $\mu$ l) of solution was drop-casted onto to the thermal electronic chip. A second chip with a SiN<sub>x</sub> membrane is located on top of the thermal E-chip in the TEM holder, producing a thin gas cavity sealed with small o-rings maintaining the high vacuum in the TEM column. The *in situ* observations were carried out at a pressure of 1 atm (760 torr) under Ar, with a flow rate of 0.1 ml min<sup>-1</sup>. The heating was carried out from room temperature up to 900 °C at a rate of 5 °C/min. To minimize the effects of the electron beam, a beam shutter was closed during thermal ramps, in order to reduce the particles exposure to the beam. In addition, areas outside the *in situ* observation zones were systematically observed for comparison, to check for any significant artefacts caused by electron irradiation.

*X-ray photoemission spectroscopy (XPS)*: XPS spectra were recorded using an ESCALAB 250 spectrometer from Thermofisher Scientific, fitted with a microfocused, monochromatic Al K $\alpha$  X-ray source ( $h\nu = 1486.6$  eV; spot size = 400 micrometers). The pass energy was set at 150 and 40 eV for the survey and the narrow regions, respectively. Spectral calibration was determined by setting the main C1s (C-C, C-H) component at 285 eV.

*Time of flight secondary ion mass spectrometry (ToF-SIMS)*: Chemical characterisation of samples was carried out by using a TOF.SIMS<sup>5</sup> instrument (IONTOF GmbH, Münster, Germany). A pulsed Bi<sup>5+</sup> metal ion source was used to produce a primary beam using an acceleration voltage of 30 kV. An AC target current of 0.035 pA with a bunched pulse width lower than 1 ns was used. Both positive and negative secondary ion species were analysed. For spectra, a raster of 128 x 128 data points over an area of 250 x 250  $\mu$ m<sup>2</sup> was used. The total primary ion beam dose for each analysed area was always kept below 4 10<sup>10</sup> ions.cm<sup>-2</sup>, ensuring static conditions. Lateral resolution of  $\sim 3$   $\mu$ m and mass resolution  $m/\Delta m > 4500$  at 29 m/z were maintained for positive and negative spectra acquisition. Charge compensation was done by an interlaced electron flood gun ( $E_k = 20$  eV). All data analyses were carried out using the software supplied by the instrument manufacturer, SurfaceLab (version 6.8). Sample powders were pressed onto adhesive part of Post-it<sup>®</sup> papers.

*Thermo gravimetric analysis coupled with in situ gas chromatography mass spectrometry and infrared spectroscopy*: Thermogravimetric analyses were performed using a Setaram labsyseo under helium from room temperature to 1000 °C with a temperature ramp of 5 K

min<sup>-1</sup>. The FTIR spectra of evolved gaseous products during TG analysis was recorded using an Infra-Red Spectrometer Thermoscientific Is 10, and gaseous products evolved were also analyzed using Gas Chromatograph-Mass Spectrometer (GC-MS) Thermoscientific Trace1310 ISQ-QD.

*CO oxidation catalysis:* CO oxidation was performed using Catlab (Hiden) that consists in a temperature controlled microreactor in which the catalyst and the reactive gas mixture may interact. The reactor is coupled with a quadrupole mass spectrometer (QGA, Hiden) for the detection of the gaseous catalysis products. The reactive gas flow employed for the catalytic test was the following; 40 ml/min of 5% O<sub>2</sub> in helium and 5 ml/min of 20 % CO in helium. This mixture ensures an excess of oxygen (2 ml/min O<sub>2</sub> and 1 ml/min CO diluted in He) to perform CO oxydation. A temperature ramp (10 °C / min) is applied from 50 °C to 250 °C and gas mixture evolution is followed by mass spectroscopy. The quantity of produced CO<sub>2</sub> as a function of the reaction temperature is calculated based on the partial pressures of CO and O<sub>2</sub> in the reactor.

For a qualitative comparison of the performance of the catalysts, the CO<sub>2</sub> signal is used, normalized by the helium signal. By assuming 100 % conversion of CO when the signal of CO<sub>2</sub> has reached its maximum, the T<sub>50</sub> (temperature at which 50 % conversion of CO occurs) can be determined.

### **Acknowledgements**

The authors thank D. Montero and the Institut des Matériaux de Paris Centre (IMPC FR2482) for servicing FEGSEM & EDX instrumentation and Sorbonne Université, CNRS and C'Nano projects of the Région Ile-de-France for funding.

The authors aknowledge Jean-Marc Krafft and the Laboratoire de Réactivité de Surface for Raman spectroscopy experiments.

Philippe Decorse is gratefully acknowledged for XPS experiments and Ivonne Cocca for ED-XRF measurements. We acknowledge the ITODYS XPS-UPS, TGA-GC-MS and SEM facilities (Université de Paris, CNRS UMR 7086, Paris, France).

The authors thank the METSA network for the access to the *in-situ* STEM-EDX facilities

**Supporting Information:** The Supporting Information is available free of charge at the publisher website. Supplemental characterization includes: SEM, TEM, XRD, IR and Raman spectra, XPS, catalysis test.

#### AUTHOR INFORMATION

##### **Corresponding Author**

##### **Marco Faustini**

Laboratoire Chimie de la Matière Condensée de Paris (LCMCP)  
Sorbonne Université–CNRS  
4, Place Jussieu, 75005 Paris, France

**Email:** marco.faustini@sorbonne-universite.fr

##### **Jennifer Peron**

Université Paris Cité, CNRS, ITODYS, F-75013 Paris, France  
Email: jennifer.peron@u-paris.fr

##### **Authors**

##### **M.L. De Marco, R. Haddad, M. Odziomek,† C. Boissière**

Laboratoire Chimie de la Matière Condensée de Paris (LCMCP)  
Sorbonne Université–CNRS  
4, Place Jussieu, 75005 Paris, France

##### **W. Baaziz, S. A. Sharna, O. Ersen**

Institut de Physique et de Chimie des Matériaux de Strasbourg (IPCMS),  
Université de Strasbourg–CNRS  
23, Rue du Loess, 67200 Strasbourg, France

##### **F. Devred, C. Poleunis, D. P. Debecker**

Institute of Condensed Matter and Nanosciences (IMCN), Université catholique de Louvain (UCLouvain),  
1, Place Louis Pasteur, 1348 Louvain-la-Neuve, Belgium

**A. Chevillot-Biraud, S. Nowak**

Université Paris Cité, CNRS, ITODYS, F-75013 Paris, France

### **Present Addresses**

†If an author's address is different than the one given in the affiliation line, this information may be included here.

### **Author Contributions**

The manuscript was written through contributions of all authors. All authors have given approval to the final version of the manuscript.

### **Funding Sources**

This work was supported by the European Research Council (ERC) under European Union's Horizon 2020 Programme (Grant Agreement No. 803220, TEMPORE).

## REFERENCES

- (1) Xin, Y.; Li, S.; Qian, Y.; Zhu, W.; Yuan, H.; Jiang, P.; Guo, R.; Wang, L. High-Entropy Alloys as a Platform for Catalysis: Progress, Challenges, and Opportunities. *ACS Catal.* **2020**, *10*, 11280–11306.
- (2) Wu, D.; Kusada, K.; Yamamoto, T.; Toriyama, T.; Matsumura, S.; Gueye, I.; Seo, O.; Kim, J.; Hiroi, S.; Sakata, O.; Kawaguchi, S.; Kubota, Y.; Kitagawa, H. On the Electronic Structure and Hydrogen Evolution Reaction Activity of Platinum Group Metal-Based High-Entropy-Alloy Nanoparticles. *Chem. Sci.* **2020**, *11*, 12731–12736.
- (3) Yeh, J.-W.; Chen, S.-K.; Lin, S.-J.; Gan, J.-Y.; Chin, T.-S.; Shun, T.-T.; Tsau, C.-H.; Chang, S.-Y. Nanostructured High-Entropy Alloys with Multiple Principal Elements: Novel Alloy Design Concepts and Outcomes. *Adv. Eng. Mater.* **2004**, *6*, 299–303.
- (4) Hsu, C.-Y.; Yeh, J.-W.; Chen, S.-K.; Shun, T.-T. Wear Resistance and High-Temperature Compression Strength of Fcc CuCoNiCrAl<sub>0.5</sub>Fe Alloy with Boron Addition. *Metall. and Mat. Trans. A* **2004**, *35*, 1465–1469.
- (5) Yao, Y.; Liu, Z.; Xie, P.; Huang, Z.; Li, T.; Morris, D.; Finfrock, Z.; Zhou, J.; Jiao, M.; Gao, J.; Mao, Y.; Miao, J.; Zhang, P.; Shahbazian-Yassar, R.; Wang, C.; Wang, G.; Hu, L. Computationally Aided, Entropy-Driven Synthesis of Highly Efficient and Durable Multi-Elemental Alloy Catalysts. *Sci. Adv.* **2020**, *6*, eaz0510: 1-10.
- (6) Xie, P.; Yao, Y.; Huang, Z.; Liu, Z.; Zhang, J.; Li, T.; Wang, G.; Shahbazian-Yassar, R.; Hu, L.; Wang, C. Highly Efficient Decomposition of Ammonia Using High-Entropy Alloy Catalysts. *Nat. Commun.* **2019**, *10*, 4011: 1-12.
- (7) Miracle, D. B.; Senkov, O. N. A Critical Review of High Entropy Alloys and Related Concepts. *Acta Mater.* **2017**, *122*, 448–511.
- (8) Peker, A.; Johnson, W. L. A Highly Processable Metallic Glass: Zr<sub>41.2</sub> Ti<sub>13.8</sub> Cu<sub>12.5</sub> Ni<sub>10.0</sub> Be<sub>22.5</sub>. *Appl. Phys. Lett.* **1993**, *63*, 2342–2344.
- (9) Furukawa, S.; Komatsu, T.; Shimizu, K. Catalyst Design Concept Based on a Variety of Alloy Materials: A Personal Account and Relevant Studies. *J. Mater. Chem. A* **2020**, *8*, 15620–15645.
- (10) Li, H.; Han, Y.; Zhao, H.; Qi, W.; Zhang, D.; Yu, Y.; Cai, W.; Li, S.; Lai, J.; Huang, B.; Wang, L. Fast Site-to-Site Electron Transfer of High-Entropy Alloy Nanocatalyst Driving Redox Electrocatalysis. *Nat. Commun.* **2020**, *11*, 5437: 1-9.
- (11) Batchelor, T. A. A.; Pedersen, J. K.; Winther, S. H.; Castelli, I. E.; Jacobsen, K. W.; Rossmeisl, J. High-Entropy Alloys as a Discovery Platform for Electrocatalysis. *Joule* **2019**, *3*, 834–845.
- (12) Yao, Y.; Dong, Q.; Brozena, A.; Luo, J.; Miao, J.; Chi, M.; Wang, C.; Kevrekidis, I. G.; Ren, Z. J.; Greeley, J.; Wang, G.; Anapolsky, A.; Hu, L. High-Entropy Nanoparticles: Synthesis-Structure-Property Relationships and Data-Driven Discovery. *Science* **2022**, *376*, eabn3103: 1-11.

- (13) Qiu, H.-J.; Fang, G.; Wen, Y.; Liu, P.; Xie, G.; Liu, X.; Sun, S. Nanoporous High-Entropy Alloys for Highly Stable and Efficient Catalysts. *J. Mater. Chem. A* **2019**, *7*, 6499–6506.
- (14) Nellaiappan, S.; Katiyar, N. K.; Kumar, R.; Parui, A.; Malviya, K. D.; Pradeep, K. G.; Singh, A. K.; Sharma, S.; Tiwary, C. S.; Biswas, K. High-Entropy Alloys as Catalysts for the CO<sub>2</sub> and CO Reduction Reactions: Experimental Realization. *ACS Catal.* **2020**, *10*, 3658–3663.
- (15) Liu, M.; Zhang, Z.; Okejiri, F.; Yang, S.; Zhou, S.; Dai, S. Entropy-Maximized Synthesis of Multimetallic Nanoparticle Catalysts via a Ultrasonication-Assisted Wet Chemistry Method under Ambient Conditions. *Adv. Mater. Interfaces* **2019**, *6*, 1900015: 1-6.
- (16) Cai, Z.-X.; Goou, H.; Ito, Y.; Tokunaga, T.; Miyauchi, M.; Abe, H.; Fujita, T. Nanoporous Ultra-High-Entropy Alloys Containing Fourteen Elements for Water Splitting Electrocatalysis. *Chem. Sci.* **2021**, *12*, 11306–11315.
- (17) Qiu, H.-J.; Fang, G.; Gao, J.; Wen, Y.; Lv, J.; Li, H.; Xie, G.; Liu, X.; Sun, S. Noble Metal-Free Nanoporous High-Entropy Alloys as Highly Efficient Electrocatalysts for Oxygen Evolution Reaction. *ACS Mater. Lett.* **2019**, *1*, 526–533.
- (18) Yao, Y.; Huang, Z.; Xie, P.; Lacey, S. D.; Jacob, R. J.; Xie, H.; Chen, F.; Nie, A.; Pu, T.; Rehwoldt, M.; Yu, D.; Zachariah, M. R.; Wang, C.; Shahbazian-Yassar, R.; Li, J.; Hu, L. Carbothermal Shock Synthesis of High-Entropy-Alloy Nanoparticles. *Science* **2018**, *359*, 1489–1494.
- (19) Yang, Y.; Song, B.; Ke, X.; Xu, F.; Bozhilov, K. N.; Hu, L.; Shahbazian-Yassar, R.; Zachariah, M. R. Aerosol Synthesis of High Entropy Alloy Nanoparticles. *Langmuir* **2020**, *36*, 1985–1992.
- (20) Wang, X.; Dong, Q.; Qiao, H.; Huang, Z.; Saray, M. T.; Zhong, G.; Lin, Z.; Cui, M.; Brozena, A.; Hong, M.; Xia, Q.; Gao, J.; Chen, G.; Shahbazian-Yassar, R.; Wang, D.; Hu, L. Continuous Synthesis of Hollow High-Entropy Nanoparticles for Energy and Catalysis Applications. *Adv. Mater.* **2020**, *32*, 2002853: 1-8.
- (21) Löffler, T.; Meyer, H.; Savan, A.; Wilde, P.; Garzón Manjón, A.; Chen, Y.-T.; Ventosa, E.; Scheu, C.; Ludwig, A.; Schuhmann, W. Discovery of a Multinary Noble Metal-Free Oxygen Reduction Catalyst. *Adv. Energy Mater.* **2018**, *8*, 1802269: 1-7.
- (22) Wu, D.; Kusada, K.; Yamamoto, T.; Toriyama, T.; Matsumura, S.; Kawaguchi, S.; Kubota, Y.; Kitagawa, H. Platinum-Group-Metal High-Entropy-Alloy Nanoparticles. *J. Am. Chem. Soc.* **2020**, *142*, 13833–13838.
- (23) Broge, N. L. N.; Bondesgaard, M.; Søndergaard-Pedersen, F.; Roelsgaard, M.; Iversen, B. B. Autocatalytic Formation of High-Entropy Alloy Nanoparticles. *Angew. Chem. Int. Ed.* **2020**, *132*, 22104–22108.
- (24) Faustini, M.; Nicole, L.; Ruiz-Hitzky, E.; Sanchez, C. History of Organic-Inorganic Hybrid Materials: Prehistory, Art, Science, and Advanced Applications. *Adv. Funct. Mater.* **2018**, *28*, 1704158: 1-30.

- (25) Kim, J.; Kani, K.; Kim, J.; Yeon, J. S.; Song, M.-K.; Jiang, B.; Na, J.; Yamauchi, Y.; Park, H. S. Mesoporous Rh Nanoparticles as Efficient Electrocatalysts for Hydrogen Evolution Reaction. *J. Ind. Eng. Chem.* **2021**, *96*, 371–375.
- (26) Li, C.; Iqbal, M.; Lin, J.; Luo, X.; Jiang, B.; Malgras, V.; Wu, K. C.-W.; Kim, J.; Yamauchi, Y. Electrochemical Deposition: An Advanced Approach for Templated Synthesis of Nanoporous Metal Architectures. *Acc. Chem. Res.* **2018**, *51*, 1764–1773.
- (27) Elmaalouf, M.; Odziomek, M.; Duran, S.; Gayrard, M.; Bahri, M.; Tard, C.; Zitolo, A.; Lassalle-Kaiser, B.; Piquemal, J.-Y.; Ersen, O.; Boissière, C.; Sanchez, C.; Giraud, M.; Faustini, M.; Peron, J. The Origin of the High Electrochemical Activity of Pseudo-Amorphous Iridium Oxides. *Nat. Commun.* **2021**, *12*, 3935: 1-10.
- (28) Smeets, V.; Boissiere, C.; Sanchez, C.; Gaigneaux, E.; Peeters, E.; Sels, B. F.; Dusslier, M.; Debecker, D. P. Aerosol Route to TiO<sub>2</sub>–SiO<sub>2</sub> Catalysts with Tailored Pore Architecture and High Epoxidation Activity. *Chem. Mater.* **2019**, *31*, 1610–1619.
- (29) Boissiere, C.; Grosso, D.; Chaumonnot, A.; Nicole, L.; Sanchez, C. Aerosol Route to Functional Nanostructured Inorganic and Hybrid Porous Materials. *Adv. Mater.* **2011**, *23*, 599–623.
- (30) Vivian, A.; Soumoy, L.; Fusaro, L.; Louette, P.; Felten, A.; Fiorilli, S.; Debecker, D. P.; Aprile, C. The High Activity of Mesoporous Ga-SiO<sub>2</sub> Catalysts in the Upgrading of Glycerol to Solketal Explained by in-Depth Characterization. *J. Catal.* **2021**, *400*, 83–92.
- (31) Boissière, C.; Nicole, L.; Gervais, C.; Babonneau, F.; Antonietti, M.; Amenitsch, H.; Sanchez, C.; Grosso, D. Nanocrystalline Mesoporous  $\gamma$ -Alumina Powders “UPMC1 Material” Gathers Thermal and Chemical Stability with High Surface Area. *Chem. Mater.* **2006**, *18*, 5238–5243.
- (32) Debecker, D. P.; Le Bras, S.; Boissière, C.; Chaumonnot, A.; Sanchez, C. Aerosol Processing: A Wind of Innovation in the Field of Advanced Heterogeneous Catalysts. *Chem. Soc. Rev.* **2018**, *47*, 4112–4155.
- (33) Odziomek, M.; Bahri, M.; Boissiere, C.; Sanchez, C.; Lassalle-Kaiser, B.; Zitolo, A.; Ersen, O.; Nowak, S.; Tard, C.; Giraud, M.; Faustini, M.; Peron, J. Aerosol Synthesis of Thermally Stable Porous Noble Metals and Alloys by Using Bi-Functional Templates. *Mater. Horiz.* **2020**, *7*, 541–550.
- (34) Yusenko, K. V.; Riva, S.; Carvalho, P. A.; Yusenko, M. V.; Arnaboldi, S.; Sukhikh, A. S.; Hanfland, M.; Gromilov, S. A. First Hexagonal Close Packed High-Entropy Alloy with Outstanding Stability under Extreme Conditions and Electrocatalytic Activity for Methanol Oxidation. *Scr. Mater.* **2017**, *138*, 22–27.
- (35) Rouquerol, F.; Rouquerol, J.; Sing, K. Adsorption by Powders and Porous Solids. Academic Press, 1999.

- (36) Ferrari, A. C.; Meyer, J. C.; Scardaci, V.; Casiraghi, C.; Lazzeri, M.; Mauri, F.; Piscanec, S.; Jiang, D.; Novoselov, K. S.; Roth, S.; Geim, A. K. Raman Spectrum of Graphene and Graphene Layers. *Phys. Rev. Lett.* **2006**, *97*, 187401: 1-4.
- (37) Tuinstra, F.; Koenig, J. L. Raman Spectrum of Graphite. *J. Chem. Phys.* **1970**, *53*, 1126–1130.
- (38) Cheng, J.; Pan, Y.; Yao, J.; Wang, X.; Pan, F.; Jiang, J. Mechanisms and Kinetics Studies on the Thermal Decomposition of Micron Poly (Methyl Methacrylate) and Polystyrene. *J. Loss Prev. Process Ind.* **2016**, *40*, 139–146.
- (39) Barnighausen; H. Handa. B.K. Die Kristallstruktur von Rhodium(III)-chlorid PDF 00- 048-0414. *J. Less-Common Met.* **1964**, *6*, 226-231.
- (40) Stroganov, E. V.; Ovchinnikov, K. V. The Crystal Structure of Ruthenium Trichloride PDF 01-085-0528. *Seriya 4: Fizika, Khimiya* **1957**, *22*, 152–157.
- (41) Belli Dell'Amico, D.; Calderazzo, F.; Marchetti, F.; Ramello, S. Molecular Structure of [Pd<sub>6</sub>Cl<sub>12</sub>] in Single Crystals Chemically Grown at Room Temperature PDF 04-007-2561 *Angew. Chem. Int. Ed.* **1996**, *35*, 1331–1333.
- (42) Kaya, A.; Kösem, G.; Yener, M.; Tav, C.; Yahsi, U.; Esmer, K. Structural and Dielectrical Properties of PMMA/TiO<sub>2</sub> Composites in Terms of Free Volume Defects Probed by Positron Annihilation Lifetime Spectroscopy. *Polym. Polym. Compos.* **2021**, *29*, 107–116.
- (43) Wu, X.; Takeshita, S.; Tadumi, K.; Dong, W.; Horiuchi, S.; Niino, H.; Furuya, T.; Yoda, S. Preparation of Noble Metal/Polymer Nanocomposites via in Situ Polymerization and Metal Complex Reduction. *Mater. Chem. Phys.* **2019**, *222*, 300–308.
- (44) Mi, J.-L.; Shen, Y.; Becker, J.; Bremholm, M.; Iversen, B. B. Controlling Allotropy in Ruthenium Nanoparticles: A Pulsed-Flow Supercritical Synthesis and in Situ Synchrotron X-ray Diffraction Study. *J. Phys. Chem. C* **2014**, *118*, 11104–11110.
- (45) Bondesgaard, M.; Broge, N. L. N.; Mamakhel, A.; Bremholm, M.; Iversen, B. B. General Solvothermal Synthesis Method for Complete Solubility Range Bimetallic and High-Entropy Alloy Nanocatalysts. *Adv. Funct. Mater.* **2019**, *29*, 1905933: 1-9.
- (46) Bondesgaard, M.; Mamakhel, A.; Becker, J.; Kasai, H.; Philippot, G.; Bremholm, M.; Iversen, B. Supercritical Flow Synthesis of Pt<sub>1-x</sub>Ru<sub>x</sub> Nanoparticles: Comparative Phase Diagram Study of Nanostructure versus Bulk. *Chem. Mater* **2017**, *29*, 3265–3273.
- (47) <https://webbook.nist.gov/cgi/inchi?ID=C7732185&Type=IR-SPEC&Index=0>. Water Infrared Spectrum. *NIST/EPA Gas-Phase Infrared Database* **2022**.
- (48) Silverstein, R. M.; Webster, F. X.; Kiemle, D. J. *Spectrometric Identification of Organic Compounds*, 7th Edition.; John Wiley & Sons, Inc, **2005**.

- (49) Gayrard, M.; Chancerel, F.; De Marco, M. L.; Naumenko, D.; Boissière, C.; Rozes, L.; Amenitsch, H.; Peron, J.; Cattoni, A.; Faustini, M. Block-Copolymers Enable Direct Reduction and Structuration of Noble Metal-Based Films. *Small* **2021**, 2104204: 1-14.
- (50) Jiang, B.; Li, C.; Dag, Ö.; Abe, H.; Takei, T.; Imai, T.; Hossain, Md. S. A.; Islam, Md. T.; Wood, K.; Henzie, J.; Yamauchi, Y. Mesoporous Metallic Rhodium Nanoparticles. *Nat. Commun.* **2017**, 8, 15581: 1-8.
- (51) Lambert, C. K. Current State of the Art and Future Needs for Automotive Exhaust Catalysis. *Nat. Catal.* **2019**, 2, 554–557.
- (52) Ding, K.; Gulec, A.; Johnson, A. M.; Schweitzer, N. M.; Stucky, G. D.; Marks, L. D.; Stair, P. C. Identification of Active Sites in CO Oxidation and Water-Gas Shift over Supported Pt Catalysts. *Science* **2015**, 350, 189–192.
- (53) Getsoian, A. (Bean); Theis, J. R.; Paxton, W. A.; Lance, M. J.; Lambert, C. K. Remarkable Improvement in Low Temperature Performance of Model Three-Way Catalysts through Solution Atomic Layer Deposition. *Nat. Catal.* **2019**, 2, 614–622.
- (54) Ivanova, S.; Petit, C.; Pitchon, V. Application of Heterogeneous Gold Catalysis with Increased Durability: Oxidation of CO and Hydrocarbons at Low Temperature. *Gold Bull.* **2006**, 39, 3–8.
- (55) Xie, S.; Tan, W.; Wang, C.; Arandiyani, H.; Garbrecht, M.; Ma, L.; Ehrlich, S. N.; Xu, P.; Li, Y.; Zhang, Y.; Collier, S.; Deng, J.; Liu, F. Structure-Activity Relationship of Pt Catalyst on Engineered Ceria-Alumina Support for CO Oxidation. *J. Catal.* **2022**, 405, 236–248.
- (56) Gu, D.; Tseng, J.-C.; Weidenthaler, C.; Bongard, H.-J.; Spliethoff, B.; Schmidt, W.; Soulimani, F.; Weckhuysen, B. M.; Schüth, F. Gold on Different Manganese Oxides: Ultra-Low-Temperature CO Oxidation over Colloidal Gold Supported on Bulk-MnO<sub>2</sub> Nanomaterials. *J. Am. Chem. Soc.* **2016**, 138, 9572–9580.
- (57) Hatton, B.; Mishchenko, L.; Davis, S.; Sandhage, K. H.; Aizenberg, J. Assembly of Large-Area, Highly Ordered, Crack-Free Inverse Opal Films. *PNAS* **2010**, 107, 10354–10359.
- (58) Protochips. Protochips Atmosphere. <https://www.protochips.com/products/atmosphere/> **2022**.